

# Nonlinear optical contrast enhancement for optical coherence tomography

**Claudio Vinegoni, Jeremy S. Bredfeldt, and Daniel L. Marks**

*Beckman Institute for Advanced Science and Technology, University of Illinois at  
Urbana-Champaign*

**Stephen A. Boppart**

*Department of Electrical and Computer Engineering  
Beckman Institute for Advanced Science and Technology, Department of Bioengineering  
College of Medicine  
University of Illinois at Urbana-Champaign, 405 N. Mathews Ave., Urbana, IL 61801  
[boppart@uiuc.edu](mailto:boppart@uiuc.edu)*

<http://nb.beckman.uiuc.edu/biophotonics/>

**Abstract:** We present a new interferometric technique for measuring Coherent Anti-Stokes Raman Scattering (CARS) and Second Harmonic Generation (SHG) signals. Heterodyne detection is employed to increase the sensitivity in both CARS and SHG signal detection, which can also be extended to different coherent processes. The exploitation of the mentioned optical nonlinearities for molecular contrast enhancement in Optical Coherence Tomography (OCT) is presented. Numerical simulations for both coherent nonlinear processes are performed in order to determine the properties of the signal expected at the exit of the described nonlinear interferometer.

© 2018 Optical Society of America

**OCIS codes:** (111.4500) Optical coherence tomography; (300.6230) Spectroscopy, coherent anti-Stokes Raman scattering; (190.4410) Nonlinear optics, parametric processes; (120.3180) Interferometry; (040.2840) Heterodyne; (190.4160) Multiharmonic generation.

---

## References and links

1. D. Huang, E. A. Swanson, C. P. Lin, J. S. Schuman, W. G. Stinson, W. Chang, M. R. Hee, T. Flotte, K. Gregory, C. A. Puliafito, and J. G. Fujimoto, "Optical coherence tomography," *Science* **254**(5035), 1178–1181 (1991).
2. S. A. Boppart, B. E. Bouma, C. Pitris, J. F. Southern, M. E. Brezinski, and J. G. Fujimoto, "*In vivo* cellular optical coherence tomography imaging," *Nat. Med.* **4**(7), 861–5 (1998).
3. Y. Wang, Y. Zhao, Z. Chen, R. S. Windeler, and J. Nelson, "Ultrahigh-resolution optical coherence tomography by broadband continuum generation from a photonic crystal fiber," *Opt. Lett.* **28**(3 Feb 1 2003), 182–184 (2003).
4. J. G. Fujimoto, "Optical coherence tomography for ultrahigh resolution *in vivo* imaging," *Nat. Biotechnol.* **21**(11), 1361–1367 (2003).
5. T. M. Lee, A. L. Oldenburg, S. Sitafalwalla, D. L. Marks, W. Luo, F. J.-J. Toublan, K. S. Suslick, and S. A. Boppart, "Engineered microsphere contrast agents for optical coherence tomography," *Opt. Lett.* **28**(17), 1546–1548 (2003).
6. U. Morgner, W. Drexler, F. Kartner, X. Li, C. Pitris, E. Ippen, and J. Fujimoto, "Spectroscopic optical coherence tomography," *Opt. Lett.* **25**(2), 111–113 (2000).
7. K. Divakar Rao, M. A. Choma, S. Yazdanfar, A. M. Rollins, and J. A. Izatt, "Molecular contrast in optical coherence tomography by use of a pump-probe technique," *Opt. Lett.* **28**(5), 340–2 (2003).
8. J. K. Barton, J. B. Hoying, and C. J. Sullivan, "Use of microbubbles as an optical coherence tomography contrast agent," *Acad. Radiol.* **9**(Suppl 1), S52–5 (2002).
9. A. Zumbusch, G. Holtorn, and X. Sunney Xie, "Three-dimensional vibrational imaging by coherent anti-Stokes Raman scattering," *Phys. Rev. Lett.* **82**(20), 4142–5 (1999).

10. W. Dermtroeder, *Laser Spectroscopy* (Springer, 1998).
  11. J.-X. Cheng, A. Volkmer, and X. Xie, "Theoretical and experimental characterization of coherent anti-Stokes Raman scattering microscopy," *J. Opt. Soc. Am. B* **19**(6), 1363–75 (2002).
  12. M. Duncan, J. Reintjes, and T. Manuccia, "Scanning coherent anti-Stokes Raman microscope," *Opt. Lett.* **7**(8), 350–2 (1982).
  13. G. W. Wurlpel, J. M. Schins, and M. Muller, "Chemical specificity in three-dimensional imaging with multiplex coherent anti-Stokes Raman scattering microscopy," *Opt. Lett.* **27**(13), 1093–1095 (2002).
  14. M. Hashimoto, T. Araki, and S. Kawata, "Molecular vibration imaging in the fingerprint region by use of coherent anti-Stokes Raman scattering microscopy with a collinear configuration," *Opt. Lett.* **25**(24), 1768–1770 (2000).
  15. D. L. Marks and S. A. Boppart, "Nonlinear interferometric vibrational imaging: theory and simulations," Submitted; LANL E–print arXiv <http://www.arxiv.org/abs/physics/0311071> (2003).
  16. D. L. Marks, J. Bredfeldt, S. Hambir, D. Dlott, B. Kitchell, M. Gruebele, and S. A. Boppart, "Molecular species sensitive optical coherence tomography using coherent anti-Stokes Raman scattering spectroscopy," in *Coherence domain optical methods and OCT in biomedicine VII*, V.V. Tuchin, J.A. Izatt, and J.G. Fujimoto, eds., Proc. SPIE **4956**, 9–13 (2003).
  17. J. Bredfeldt, D. L. Marks, C. Vinegoni, S. Hambir, and S. A. Boppart, "Coherent anti-Stokes Raman scattering heterodyne interferometry," Submitted; LANL E–print arXiv <http://www.arxiv.org/abs/physics/0311057> (2003).
  18. P. J. Campagnola and L. M. Loew, "Second-harmonic imaging microscopy for visualizing biomolecular arrays in cells, tissues and organisms," *Nat. Biotechnol.* **21**(11), 1356–1360 (2003).
  19. P. Stoller, P. M. Celliers, K. M. Reiser, and A. M. Rubenchik, "Quantitative second-harmonic generation microscopy in collagen," *Appl. Optics* **42**(25), 5209–5219 (2003).
  20. I. Freund and M. Deutsch, "Connective tissue polarity. Optical second-harmonic microscopy, crossed-beam summation, and small-angle scattering in Rat-tail tendon," *Biophys. J.* **50**(4), 693–712 (1986).
  21. K. Eisenthal, "Liquid Interfaces Probed by Second-Harmonic and Sum-Frequency Spectroscopy," *Chem. Rev.* **96**(4), 1343–60 (1996).
  22. R. Brown, A. Millard, and P. J. Campagnola, "Macromolecular structure of cellulose studied by second-harmonic generation imaging microscopy." *Opt. Lett.* **28**(22), 2207–2209 (2003).
  23. J. Squier, M. Muller, G. Brakenhoff, and K. Wilson, "Third harmonic generation microscopy," *Opt. Express* **3**(9), 315–24 (1998).
- 

## 1. Introduction

Optical coherence tomography (OCT) is an emerging biomedical imaging technology that has been applied to a wide range of biological, medical, and materials investigations. OCT was first developed in the early 1990s for noninvasive imaging of biological tissue [1] and is capable of imaging tissue microstructures at near histological resolutions [2]. Axial resolution of 10  $\mu\text{m}$  is common for standard OCT, where for ultrahigh resolution OCT, an axial resolution in the 1  $\mu\text{m}$  range has been recently achieved using broadband-continuum generation from a photonic crystal fiber [3].

The advantages of OCT in biomedical imaging, compared to other imaging techniques, are quite numerous [4]. In particular, OCT can provide imaging resolutions that approach those of conventional histopathology and can be performed *in situ* [4]. Despite its advantages, a serious drawback to OCT is that the linear scattering properties of pathological tissue probed by OCT are often morphologically and/or optically similar to the scattering properties of normal tissue. For example, although morphological differences between normal and neoplastic tissues may be obvious at later stages of tumor development, it is frequently difficult to optically detect early-stage tumors [5].

This implies a need for novel contrast enhancing mechanisms for OCT. Examples of methods that have been recently developed, include: spectroscopic OCT [6], pump and probe techniques [7], and the use of engineered microspheres [5] or microbubbles [8]. Spectroscopic OCT (SOCT) measures the spectral absorption from tissues by measuring the spectral differences between the source and the backscattered interference signal to provide information about the properties of the scatterers in the sample. However, this technique is limited to the identification of scatterers that have absorption within the bandwidth of the optical source. Pump and probe contrast enhancement for OCT imaging relies on transient absorptions in the sample un-

der investigation that are induced by an external pump beam. Unfortunately it is necessary in most cases to introduce different contrast agents depending on the excitation source and on the transient spectra of the molecules under investigation [7]. An alternative way to obtain contrast enhancement in OCT includes the use of exogenous contrast agents such as engineered microspheres. These microspheres can be targeted to cell receptors and change the optical scattering or absorption characteristics in selected regions, providing molecular specific contrast [5].

As clearly evidenced above, most of the current methods (if not all) that are currently used to enhance contrast imaging in OCT require the presence of a contrast agent, which can modify the biology under investigation. It follows there is a need for new techniques that could help eliminate this limitation. In this paper, we propose and present new methods to achieve enhanced OCT contrast, exploiting optical nonlinearities. The nonlinear effects on which we focus in this work in particular are Coherent Anti-Stokes Raman Scattering (CARS) and Second Harmonic Generation (SHG), but the general idea could be easily extended to other nonlinear effects such as Third Harmonic Generation (THG), Coherent Stokes Raman Spectroscopy (CSRS), and stimulated emission in active materials (i.e. InGaAs, GaAs based materials, etc.).

## 2. CARS contrast enhancement

### 2.1. Theory

It is well known that the nonlinear polarization for a material can be expressed as a function of the incident electric field vector  $\vec{E}$ :

$$\vec{P} = \epsilon_0 \left( \chi^{(1)} \cdot \vec{E} + \chi^{(2)} : \vec{E}\vec{E} + \chi^{(3)} \vdots \vec{E}\vec{E}\vec{E} + \dots \right) \quad (1)$$

with  $\vec{P}$  the induced polarization,  $\chi^{(n)}$  the n-th order nonlinear susceptibility, and  $\epsilon_0$  the vacuum permittivity. This implies that for high intensities (i.e. in a nonlinear regime) the induced polarization is no longer directly proportional to the incoming electric field vector  $\vec{E}$ . Usually the first term  $\chi^{(1)}$  represents the main contribution to  $\vec{P}$  and describes linear effects as absorption or reflection. The second term is responsible for nonlinear effects like SHG and sum-frequency generation which we will consider in Sect. 3. The third term  $\chi^{(3)}$  is responsible for phenomena involving four photons, like CARS, four wave mixing (FWM), third harmonic generation (THG), and nonlinear refraction.

In this section we focus on CARS, a spectroscopic technique that has recently received increasing attention for its applications for vibrational imaging [9]. In CARS spectroscopy, the frequencies of two incident lasers,  $\omega_p$  and  $\omega_s$  (Pump and Stokes, respectively), are selected such that the difference in frequency  $\omega_p - \omega_s = \omega_v$  is equal to the frequency of a Raman-active vibrational mode present in the molecule under study [10]. As evidenced from Eq.1, CARS is a nonlinear, four-wave mixing process. It follows the CARS field is a result of the interaction between four photons and is generated in the phase-matching direction at the anti-Stokes frequency  $\omega_{AS} = 2\omega_p - \omega_s$ , implying that the CARS signal intensity is linearly dependent on the Stokes field intensity and quadratically dependent on the pump field intensity. Note that CARS is a coherent process, with the phase of the anti-Stokes field related to the phase of the excitation field. Therefore, constructive interference of the anti-Stokes field causes the CARS signal to be significantly larger than the spontaneous Raman signal, given the same average excitation power [11]. All these characteristics have allowed CARS to be successfully employed to provide vibrational contrast in scanning microscopy [9, 11, 12, 13]. CARS microscopy generally involves scanning overlapped and tightly focused pump and Stokes lasers through a sample while measuring the anti-Stokes signal amplitude point by point [14]. The first CARS microscope [12] used non-collinear pump and Stokes visible lasers to prove microscopic imaging of the spatial distribution of deuterated molecular bonds in a sample of onion skin.

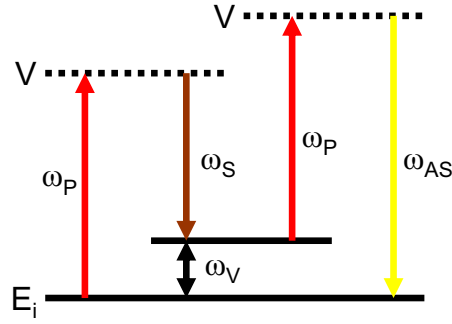


Fig. 1. Simplified energy diagram for CARS.  $\omega_p$  indicates the pump laser frequency,  $\omega_s$  the Stokes laser frequency,  $\omega_{AS}$  the Anti-Stokes frequency (emitted CARS signal), and  $\omega_v$  the Raman frequency corresponding to an active vibrational transition.

Picosecond lasers were used by Hashimoto et al.[14] to improve the Raman spectral resolution and to further reduce the non-resonant background signal. Cheng et al.[11] theoretically evaluated the use of CARS in microscopy and recently used polarization, epi-directional, counter propagating, and forward CARS microscopy to study cell biology. Multiplex CARS imaging has also been demonstrated to provide contrast based on one or more vibrational spectral features [13].

In each of these CARS microscopy techniques, the anti-Stokes photons are counted in order to estimate the density of the Raman scatterers in the focal volume of the microscope. Unfortunately, the spectral phase information is lost in this process. In this paper we present a new interferometric technique called Nonlinear Interferometric Vibrational Imaging (NIVI) [15] with the capability for heterodyne detection and the possibility to obtain a full reconstruction of the magnitude and phase of the sample Raman susceptibility [16, 17].

## 2.2. Experimental Setup

The laser system constructed to create the laser fields necessary to stimulate the CARS signal in the samples is shown in Fig.2. A diode pumped frequency doubled Nd:YVO<sub>4</sub> laser (Coherent, Verdi) was used to pump a mode-locked Ti:sapphire oscillator (KMLabs) operating at a center wavelength of 807 nm, with a bandwidth of 30 nm, a repetition rate of 82 MHz, and an average power of 300 mW. These pulses were sent to seed a regenerative chirped pulse amplifier (Coherent, RegA 9000) that produced approximately 70 fs, 5  $\mu$ J pulses with a repetition rate of 250 kHz and an average power of 1.25 W. Around ten percent of this average power was used as the pump beam; the remaining power was directed to an optical parametric amplifier (Coherent, OPA 9400) which generated a 4 mW average power Stokes beam, tunable from 400-1200 nm [17].

Once the pump and the Stokes fields were generated, the two fields entered the interferometer shown in detail in Fig.3. An excitation field consisting of two overlapped pulses centered at the pump and Stokes wavelengths was divided by a beamsplitter into two separate interferometer paths, which are referred to in Fig.3 as “sample arm” and “reference arm”.

A sample of a molecule was placed into each arm into which the split excitation fields were focused. When the Stokes pulses were tuned such that the difference in frequency between the pump and Stokes pulses was equal to a Raman active vibrational mode present in the molecule in both the sample arm and the reference arm, an anti-Stokes signal was generated in each arm

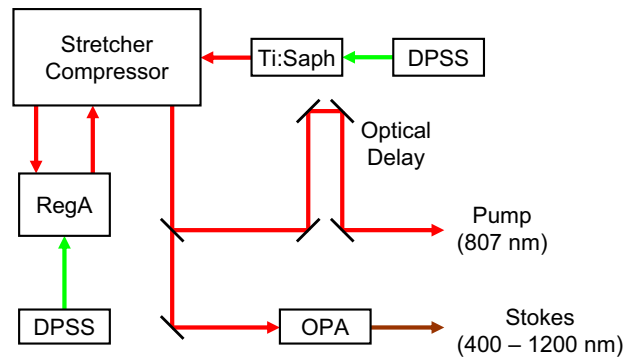


Fig. 2. Setup used to generate the Stokes and the Pump excitation fields.

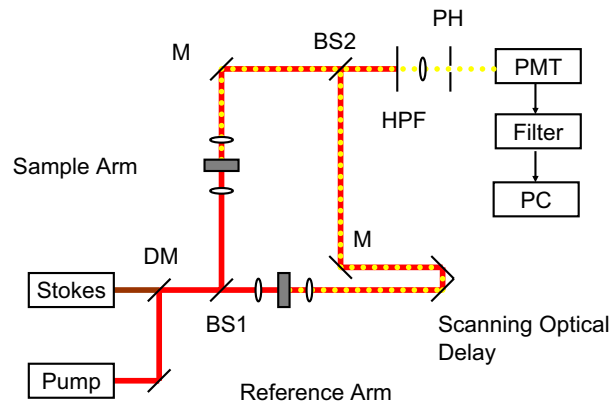


Fig. 3. Setup of the interferometric CARS measurement system [16, 17]. DM, dichroic mirror; BS, beamsplitter; M, mirror; HPF, high-pass-filter; PH, pin-hole; PMT photomultiplier tube; PC, personal computer.

of the interferometer. It will follow that the anti-Stokes fields, being coherent with the incident fields, will interfere at the beamsplitter BS2 when temporally and spatially overlapped.

The pump and Stokes pulses, at 807 and 1072 nm respectively, were used to excite the Raman-active vibrational mode of benzene at  $3063\text{ cm}^{-1}$ . The pulses were collinearly overlapped using a dichroic mirror and split with a 50:50 ultrafast beamsplitter (BS1) into the sample arm and the reference arm. The positions of the samples in the sample and reference arms were chosen such that the distances of the samples from the beamsplitter BS1 were equal. The two generated anti-Stokes pulses were then overlapped in time by adjusting the relative delay (delay line) and in space by adjusting the position on a second beamsplitter (BS2). The anti-Stokes signal was spectrally and spatially filtered. The delay line in the reference arm was scanned by a computer-controlled single axis translation stage at a constant rate. The CARS signal intensity was measured with a photomultiplier tube (PMT). The signal was filtered with a low-pass anti-aliasing filter and sampled with a PC based data acquisition system (NI DAQ, National Instruments).

### 2.3. Results and discussion

Initially the interferometer was calibrated with the pump signal only ( $\lambda = 807\text{ nm}$ ). The acquired interferogram (Fig.4) is shown for reference as a comparison with the following interferograms shown below. The interferogram was detected at the beamsplitter BS2 (Fig.3) and was recorded as the pathlength of the reference arm was scanned. Having determined the in-

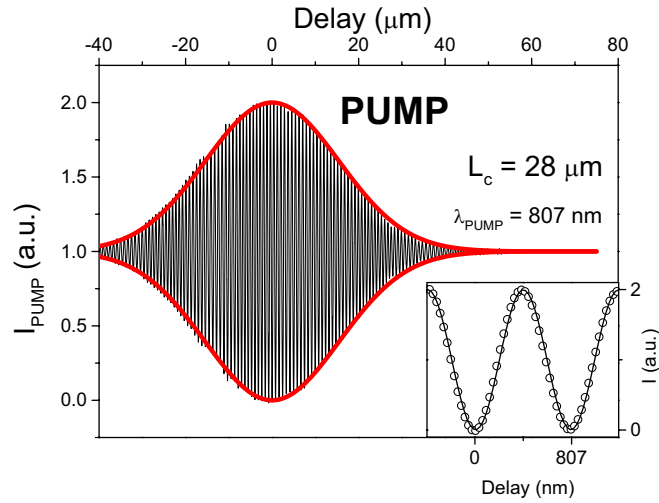


Fig. 4. Interferogram of the pump beam detected at the beamsplitter BS2 of the setup shown in Fig.3. The envelope of the interferogram was fitted using the modulus of the degree of the coherence function. In the inset is shown a detail of the interference pattern and its fit by the real part of the degree of coherence function (open circles: experimental data; solid line: fit).  $L_c$  is the coherence length of the pulse.  $\lambda_{PUMP}$  is the wavelength of the Pump signal.

terferogram for the pump field, we inserted in the two interferometer arms two quartz cuvettes filled with benzene. We first demonstrate that the signal collected from the cuvette was a CARS signal. Figs. 5(a) and 5(b) show the observed relationship between the CARS and the pump intensity (Stokes intensity fixed) and the CARS and the Stokes intensity (pump intensity fixed), respectively. In agreement with the theory, the slope of the fitted lines verify the linear relation-

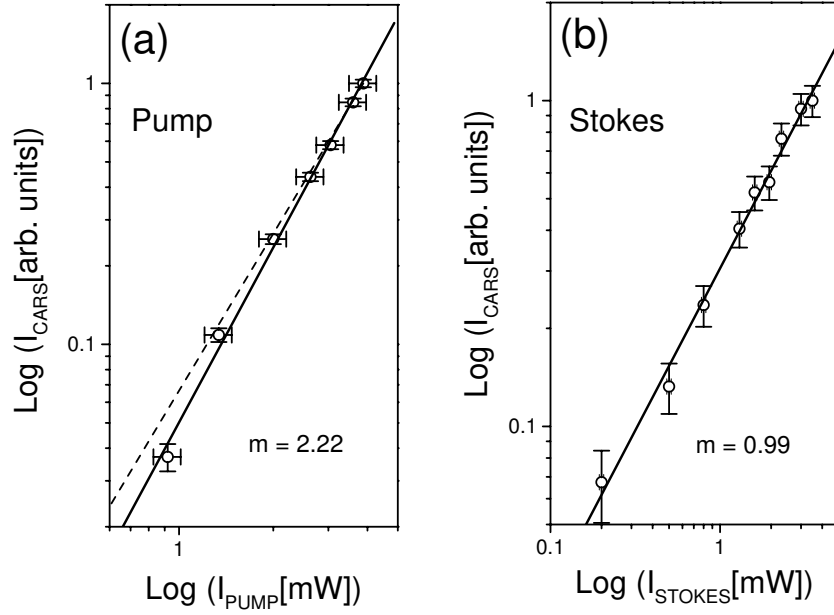


Fig. 5. Log-log plots of the intensity of the CARS signal as a function of (a) the intensity of the Pump field and (b) the intensity of the Stokes field (solid lines, curve fitting). The dotted line in (a) has a slope of 2. “m” is the angular coefficient of the solid lines [17].

ship between the anti-Stokes and the Stokes intensities, and the quadratic relationship between the anti-Stokes and the pump intensities. This implies that our signal is a result of a four-wave mixing process. In addition, we observed that this process is CARS resonance because the anti-Stokes power is maximized when the Stokes wavelength is tuned to resonance with the Raman-active benzene vibrational mode.

Established that the filtered signals from both the cuvettes were CARS signals, we detected the resulting signal at the beamsplitter BS2 of the setup shown in Fig.3. The measured interferogram results from the interference between the two anti-Stokes signals and was recorded as the pathlength of the reference arm was scanned. The function used to fit the experimental data is the degree of coherence function, that under the assumption of a Gaussian spectral distribution, is given by

$$\gamma(\tau) = \exp\left(-i\tau\omega_0 - i\frac{\delta\omega^2\tau^2}{4}\right) \quad (2)$$

where  $\tau$  is the time,  $\omega_0$  is the center frequency and  $\delta\omega$  is the bandwidth of the CARS pulse. This function is used to fit the interferogram in Fig.6. The real part and the modulus of the coherence function, under the assumption of a Gaussian spectral distribution, are used to fit the experimental data (interferogram and envelope respectively) and are plotted in Fig. 6.

The resulting coherence length  $L_C$ , defined as the axial resolution of the interferometric CARS measurement technique, is equal to

$$\tau_c = \int_{-\infty}^{+\infty} |\gamma(\tau)|^2 d\tau \quad (3)$$

and was found to be equal to 32  $\mu\text{m}$ .

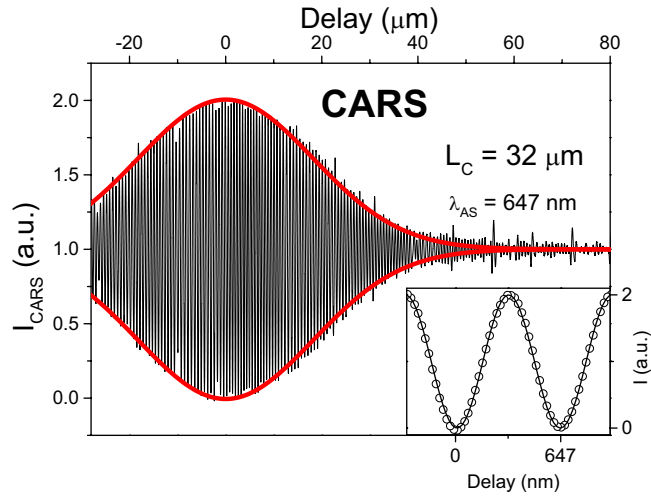


Fig. 6. CARS interferogram of the pump beam detected at the beamsplitter BS2 of the setup shown in Fig.3. The envelope of the interferogram was fitted using the modulus of the degree of the coherence function. In the inset is shown a detail of the interference pattern and its fit by the real part of the degree of coherence function (open circles: experimental data; solid line: fit).  $L_c$  is the coherence length of the pulse.  $\lambda_{AS}$  is the wavelength of the CARS signal.

The possibility to demodulate interferometrically the two anti-Stokes signals generated in separate samples demonstrates the potential of CARS as a promising technique for providing molecular contrast for OCT-like interferometric imaging systems. Interference indicates that similar Raman-active vibrational frequencies were present in both the reference and the sample arm. The “fingerprint” nature of Raman spectroscopy and the possibility to switch between different molecular species in the reference arm, could permit selective detection and imaging of different molecules in the sample.

Moreover, the possibility to interfere a weak CARS signal with another strong CARS signal (produced in the reference arm), provides heterodyne sensitivity and an improved S/N ratio.

### 3. SHG contrast enhancement

#### 3.1. Theory

Second Harmonic Generation (SHG), also known as frequency doubling, has recently emerged as a valid imaging contrast mechanism for microscopic imaging of cell and tissue structures and functions [18]. As mentioned in Sec. 2.1 SHG, in contrast to CARS, is a  $\chi^{(2)}$  process in which two photons at the fundamental frequency are converted into a single photon at exactly twice the frequency without having any absorption and/or re-emission from the sample [19]. Even in this case the intensity of the incident light is responsible for the induced nonlinear polarization, with the result that the amplitude of the SHG signal is proportional to the square of the incident light intensity.

The first biological SHG imaging experiment [18] dates back to 1986 and involved the study of orientation of collagen fibers in rat tail tendon [20]. Since then, SHG microscopy has been successfully applied in many different fields. In particular, SHG has proved to be highly effective in selectively probing interfaces, without being overwhelmed by the signal coming from



the bulk media [21]. The reason for this is that second-order processes are electric dipole forbidden in centrosymmetric media. This implies bulk liquids and centrosymmetric crystalline solids do not generate second-harmonic signals. Instead, at the interfaces, the molecular and atomic species experience different interactions and the inversion symmetry, which is present in the bulk, is broken [21]. Another advantage of SHG microscopy is the high resolution typically achieved in nonlinear microscopy, and its applications for imaging structures in live tissues consisting of endogenous proteins such as collagen. Note that the contrast mechanism is obtained without requiring the presence of any exogenous labels [22].

For all these reasons, SHG microscopy is a good candidate for providing contrast enhancement for OCT. In the next section we will demonstrate that the interferometer presented in Sec. 2.1 can be analogously used for SHG heterodyne detection due to the fact that SHG, like CARS, is a process coherent with the excitation field.

### 3.2. Experimental Setup

The SHG interferometer is similar to the CARS interferometer and is shown in Fig.7. In this

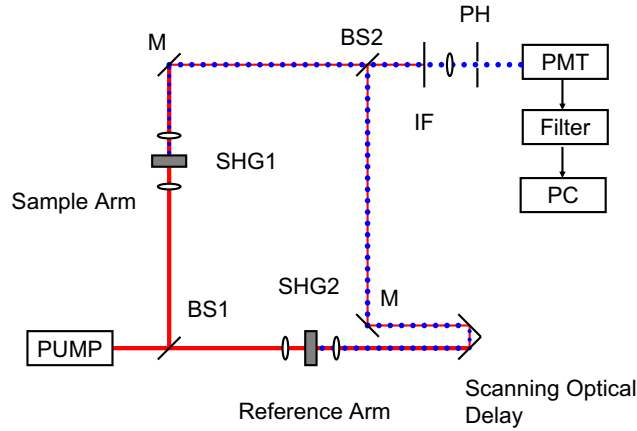


Fig. 7. Setup of the interferometric SHG measurement system. Two different SHG crystals (Type I) were inserted in the two arms of the interferometers. BS, beamsplitter; M, mirror; IF, interference filter; PH, pin-hole; PMT, photomultiplier tube; PC, personal computer.

configuration, instead of having a Stokes and a Pump laser, only the Pump laser at 807 nm was present. In the reference arm, a reference nonlinear crystal (BBO, Type I) with a thickness of 100  $\mu\text{m}$  was present in which SHG signal was created. In the sample arm, a different nonlinear crystal (BBO, Type I) with a thickness of 1 mm, was present. The signals generated in both the crystals were overlapped as in the CARS configuration scheme.

Unique to the general methodology of our technique, when a SHG crystal is placed in the reference arm, SHG signal created in the sample under investigation and present in the sample arm can be heterodyne-detected, allowing for high sensitivity detection and OCT imaging.

### 3.3. Results and discussion

Fig.8 shows the measured interferogram resulting from the interference between the two SHG signals. This result indicates that two SHG signals generated in separate samples using the same

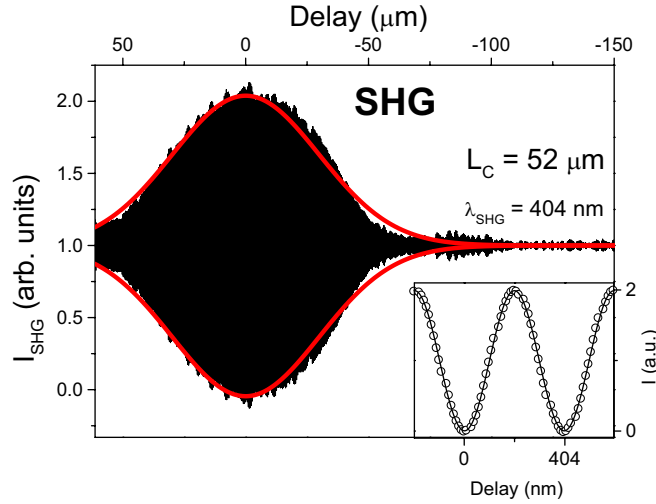


Fig. 8. SHG interferogram detected at the beamsplitter BS2 of the setup shown in Fig.7. The interferogram was recorded as the pathlength of the reference arm was scanned. The modulus of the degree of the coherence function was used to fit the envelope of the interferogram. The inset shows a detail of the interference pattern and its fit by the real part of the degree of coherence function (open circles: experimental data; solid line: fit).  $L_C$  is the coherence length of the pulse. SHG is the wavelength of the SHG signal.

pump laser can be demodulated interferometrically. In this case as well, the presence of interference clearly demonstrates the potential of SHG and resonance-enhanced SHG as a promising technique for providing molecular contrast for OCT-like interferometric imaging systems. The presence of a nonlinear crystal in the reference arm will allow one to interferometrically demodulate the SHG signal created in the sample under investigation.

#### 4. Simulations

Simulations of the coherent nonlinear processes were performed to determine the properties of the signals that could be expected from both the nonlinear interferometric setups (Fig.3, and Fig.7) utilizing SHG and CARS. Because of the wide bandwidths typically used in OCT signals, the slowly varying envelope approximation did not suffice for these simulations. Instead, we utilized a method that approximated a continuous signal by sampling it spatially at regular intervals. The evolution of the nonlinear signal was achieved by applying the nonlinearity at each point in space and time, and propagating the signal forward in time in uniform steps. Because of the low conversion efficiency, we assumed that the incident wave would not change in time except for linear propagation effects, and so would experience no depletion in energy. The model assumed that the incident and excited waves were one-dimensional plane waves. As a result, walk-off effects resulting from the divergence of the wave and ray (Poynting) vectors that occur with a finite incident beam size in a birefringent medium were not accounted for. For the simulation of SHG, the nonlinearity was assumed to be instantaneous, but the dispersion of the BBO crystal was accounted for, so that phase matching effects (at 28 degrees inclination of the extraordinary axis) were properly simulated. The incoming wave was negatively chirped, with an 807 nm center frequency and 30 nm bandwidth. Because of the rather thick crystal (1 mm) used in the experiment and present in the sample arm, 5 ps of simulation time was used to interact the waves. Due to the thickness, phase matching can not be achieved over the entire

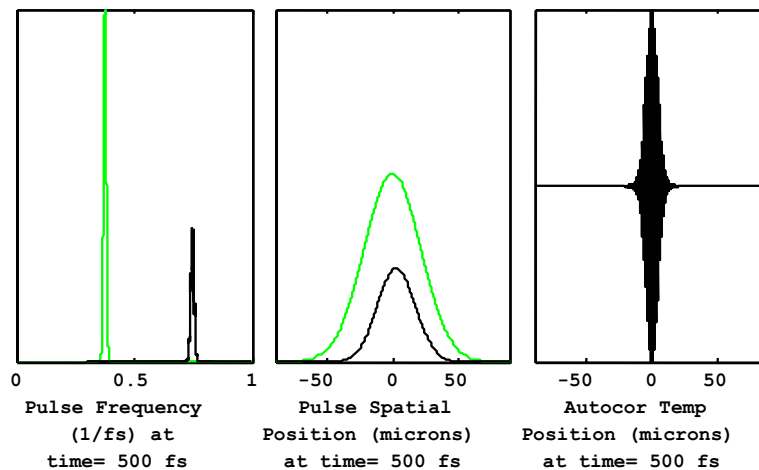


Fig. 9. Simulation of SHG. Click on figure to view an mpeg movie (817 kB) of nonlinear interferometry of the coherent SHG process.

incident bandwidth. The results of the simulation are shown in the first movie, a clip of which is shown in Fig.9. The left graph shows the temporal spectrum of the incident beam in green, and the second harmonic spectrum in black as the pulse evolves in time. The middle graph shows the spatial envelope of the incident pulse in green and the created second harmonic pulse in black. Finally, the right graph shows the autocorrelation of the second harmonic pulse at that time, which corresponds to the interferogram that would be measured from two identical BBO crystals of a thickness that corresponds to the propagation time of the simulation. The spatial origin of the simulation moves with the reference frame of the incident pulse.

For the first 500 fs, the bandwidth is approximately  $\sqrt{2}$  times that of the incident pulse. As phase mismatch and group velocity mismatch start to occur, the nonlinear polarization adds destructively with the second harmonic pulse. The resulting spectrum of the pulse becomes quite nonuniform. Because the excited signal is simulated as a plane wave, all of the generated frequency components overlap spatially and contribute to the autocorrelation of the measured interference signal. Therefore the simulated autocorrelation has many sidelobes corresponding to the nonuniform spectrum. In the experimental setup, a focused beam was used, and so the walk-off separated the spectral components of the second harmonic pulse spatially. At the pinhole PH present at the exit of the interferometer (Fig.7), only a limited bandwidth could be focused through, and so the autocorrelation length was much longer than would have been expected if phase matching occurred over the entire incident pulse bandwidth. We expect that with a shorter crystal, phase-matching could be better achieved and the autocorrelation could achieve its theoretical minimum for the bandwidth available from the incident pulse.

Simulating the CARS process require a different approach because unlike a nonresonant nonlinear second-harmonic generation process, a resonant process has a “memory” associated with the nonlinear polarization of the Raman process at each point in the medium. Walk-off did not occur because the simulated medium, liquid benzene, is isotropic. The incoming radiation was assumed to be two overlapped pulses of 30 nm bandwidth at 807 and 1072 nm, which

created a beat frequency at a vibrational frequency of the benzene. The vibration was assumed to be a single vibration of Lorentzian profile with a much longer lifetime than the duration of the incident pulse. At each time step the nonlinear Raman polarization at each point in the medium was updated by driving it with the instantaneous intensity of the incident pulse at that point. Fluctuations in the intensity of the incident field at the Raman frequency will excite the nonlinear polarization at that point in the medium. This nonlinear polarization was mixed with the incident beam to create the anti-Stokes signal. The second movie, shown in

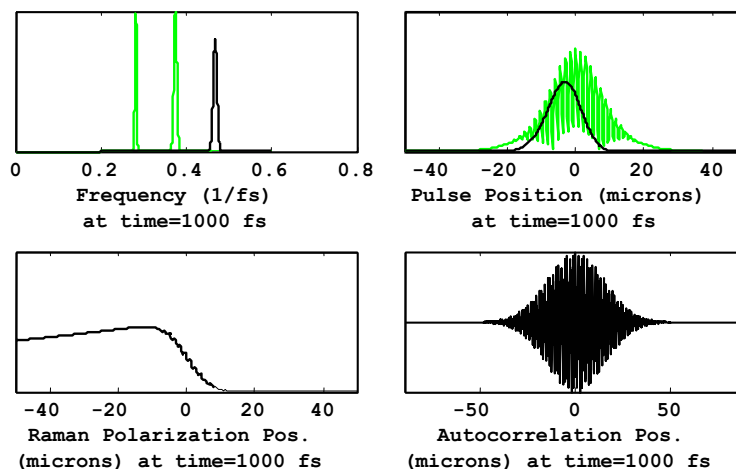


Fig. 10. Simulation of CARS. Click on figure to view an mpeg movie (1.713 Mb) of non-linear interferometry of the coherent CARS process.

Fig.10, details the evolution of the simulation of the anti-Stokes pulse in liquid benzene over 1 ps. The upper left graph shows the temporal spectrum of the incident pulse in green, and the created anti-Stokes spectrum in black. The upper right graph shows the spatial profile of the magnitude of the incident pulse in green, and the magnitude of the created anti-Stokes pulse in black. The lower left shows the spatial distribution of the magnitude of the Raman polarization of the benzene medium. Finally, the lower right shows the autocorrelation of the anti-Stokes pulse. Initially, as the pulse propagates the medium is not excited, and therefore no anti-Stokes light can be created. As the pulse moves through a given point in the medium, the medium is resonantly excited. The medium then mixes with the incoming pulse to generate an anti-Stokes wave on the trailing edge of the incident pulse, where the maximum Raman polarization coincides with the incident pulse. Because the anti-Stokes and incident pulses are close in frequency, and dispersion is low in the near infrared, the anti-Stokes pulse can remain in phase with the incident pulse for a long distance in the medium and phase matching is easier to achieve. Because of the lack of walk-off, the simulation predicts well the autocorrelation observed by experiment.

## 5. Conclusion

In conclusion, we have described a novel technique for contrast enhancement in OCT based on optical nonlinearities. The contrast mechanisms are based on resonant enhancement of the third order and second order nonlinear susceptibility of the molecules under investigation. The interference between two CARS signals generated in separate samples (or alternatively two SHG signals), was observed, allowing for heterodyne detection. Numerical simulations for both coherent nonlinear processes were performed in order to determine the properties of the signal expected at the exit of the described nonlinear interferometers, and the predicted results are in agreement with the experimental data. The proposed interferometric scheme is very promising for the development of a new molecular imaging technique (NIVI) based on nonlinear, low-coherence interferometry [15, 17] and for SHG-OCT.

In this work, we focused on forward CARS and SHG, but epi-detected CARS and SHG are coherent as well and are compatible with OCT coherence-ranging systems. CARS and SHG interferometry provide the advantages of interferometric detection and at the same time provide OCT with molecular-specific contrast. These advantages could make CARS and SHG interferometry a powerful tool for biological imaging with OCT. Moreover, the same configuration scheme could be exploited for Third Harmonic Generation (THG) microscopy [23], Coherent Stokes Raman Scattering (CSRS) microscopy, and other coherent scattering processes.

## 6. Acknowledgements

This research was supported in part by a research grant entitled "A Nonlinear OCT System for Biomolecular Detection and Intervention" from NASA and the National Cancer Institute (NAS2-02057, SAB). S.A. Boppart's email address is boppart@uiuc.edu.